scientific reports

OPEN

MoS$_2$ and Fe$_2$O$_3$ co-modify g-C$_3$N$_4$ to improve the performance of photocatalytic hydrogen production

Yan Zhang, Junfen Wan, Chunjuan Zhang & Xuejun Cao✉

Photocatalytic hydrogen production as a technology to solve energy and environmental problems exhibits great prospect and the exploration of new photocatalytic materials is crucial. In this research, the ternary composite catalyst of MoS$_2$/Fe$_2$O$_3$/g-C$_3$N$_4$ was successfully prepared by a hydrothermal method, and then a series of characterizations were conducted. The characterization results demonstrated that the composite catalyst had better photocatalytic performance and experiment results had confirmed that the MoS$_2$/Fe$_2$O$_3$/g-C$_3$N$_4$ composite catalyst had a higher hydrogen production rate than the single-component catalyst g-C$_3$N$_4$, which was 7.82 mmol g^{-1} h^{-1}, about 5 times higher than the catalyst g-C$_3$N$_4$ (1.56 mmol g^{-1} h^{-1}). The improvement of its photocatalytic activity can be mainly attributed to its enhanced absorption of visible light and the increase of the specific surface area, which provided more reactive sites for the composite catalyst. The successful preparation of composite catalyst provided more channels for carrier migration and reduced the recombination of photogenerated electrons and holes. Meanwhile, the composite catalyst also showed higher stability and repeatability.

With the rapid development of the social economy, human demand for energy is increasing. Traditional fossil energy is non-renewable, and the extensive use of fossil resources brings a serious crisis to the environment[1–3]. Therefore, it is urgent to find a kind of alternative energy to replace fossil energy. Hydrogen as a clean and renewable energy has received widespread attention. Photocatalytic hydrogen production is a technology that uses solar energy to produce hydrogen, exhibits broad prospect in solving resource and environmental pollution problems[4]. However, in the current photocatalysis research, the semiconductor catalysts show a low rate of hydrogen generation due to their various defects and cannot be widely used. Therefore, the development of efficient and stable photocatalysts has become a hot spot in current research.

In the past few decades, scholars have devoted themselves to finding semiconductor catalytic materials with high catalytic performance, semiconductor materials have been extensively explored, such as TiO$_2$[5–7], CdS[8–10], ZnO[11–13] and g-C$_3$N$_4$[14–16]. Among the various semiconductor catalysts that have been currently developed and researched, g-C$_3$N$_4$, as a non-metal semiconductor material, has attracted wide attention because of its suitable band gap, good stability, and visible light response. However, its small specific surface area and strong photo-generated electron–hole recombination ability hinder its hydrogen production performance[17–19]. Many methods have been adopted in the current research to improve the performance of the semiconductor catalyst g-C$_3$N$_4$ and increase its hydrogen production rate. For example, using doped metal and non-metal elements to accelerate the separation of charges[20–23], changing the structure of g-C$_3$N$_4$ to increase its specific surface area[24], forming a heterojunction with other materials[25–27], or supporting cocatalysts to accelerate electron transfer [28].

Hematite (α-Fe$_2$O$_3$), as a transition metal oxide with a band gap of 2.0–2.2 eV, has been explored extensively. Because of its various forms, high photocurrent density and good thermodynamic stability, it was used widely in photocatalysis research[29]. A lot of studies have been conducted to form a heterojunction between Fe$_2$O$_3$ and g-C$_3$N$_4$[30–32], and the results confirmed that when the heterojunction was formed, the electrons of Fe$_2$O$_3$ can be transferred to the conduction band of g-C$_3$N$_4$ to consume holes under light conditions, thus reducing the electron-holes recombination in g-C$_3$N$_4$ to improve the catalytic activity of composite catalysts. MoS$_2$ is a transition metal sulfide with a band gap of about 1.9 eV, has a wide spectral absorption range and can provide migration channels for carriers[33]. Previous studies have proved that MoS$_2$ is an effective cocatalyst that can significantly

State Key Laboratory of Bioreactor Engineering, East China University of Science and Technology, 130 Meilong Rd., Shanghai 200237, China. ✉email: caoxj@ecust.edu.cn

improve the photocatalytic activity of g-C$_3$N$_4$[34]. However, the photocatalytic hydrogen production rate of the MoS$_2$/g-C$_3$N$_4$ composite catalyst is still relatively low.

At present, there were many works on the composite catalysts of Fe$_2$O$_3$/g-C$_3$N$_4$[30,31] and MoS$_2$/g-C$_3$N$_4$[33,35], but the combination of binary composite catalysts still has the problem of low catalytic rate, so in this research, we combined g-C$_3$N$_4$ with Fe$_2$O$_3$ and MoS$_2$ to synthesize a new ternary composite catalyst by hydrothermal method to further improve the rate of catalysis. After exploring the addition ratio of Fe$_2$O$_3$ and MoS$_2$, the best ratio of composite catalyst was determined. The increase in the specific surface area of the composite catalyst provided more reaction sites for the photocatalytic reaction. The addition of Fe$_2$O$_3$ and MoS$_2$ accelerated the migration of carriers and the separation of photogenerated electrons and holes. The hydrogen production rate of the composite catalyst was 7.82 mmol g^{-1} h^{-1}, which was 5 times higher than the basic catalyst g-C$_3$N$_4$. Besides, this article also explored the photocatalytic mechanism and stability of the composite catalyst.

Experimental method

Synthesis of photocatalysts. Melamine (99%), (NH$_4$)$_2$CO$_3$ and Fe(NO$_3$)$_3$.9H$_2$O(> 98%) were purchased from Sinopharm Chemical Reagent Co., Ltd. Na$_2$MoO$_4$·2H$_2$O was purchased from Jiu ding chemical Technology Co., Ltd. L-cysteine and Chloroplatinic acid hexahydrate (H$_2$PtCl$_6$·6H$_2$O) were purchased from Macklin Biochemical Co., Ltd. Lactic acid was purchased from Ling feng Chemical Reagent Co., Ltd. All reagents are not treated separately.

Preparation of g-C$_3$N$_4$: In general, melamine was used as a precursor in a muffle furnace to synthesize g-C$_3$N$_4$ in an air atmosphere. 5 g melamine was put in a crucible with a lid and calcined at 550 °C for 4 h, with a heating rate of 2.5 °C/min. After the calcination was completed, it was cooled and ground the obtained lump g-C$_3$N$_4$ to obtain light yellow powder, denoted as CN.

Preparation of MoS$_2$: Typically, 1.21 g Na$_2$MoO$_4$·2H$_2$O and 1.56 g L-cysteine were dissolved in 50 mL deionized water, stirred for 30 min to fully dissolve the solid. Then the solution was diverted to an autoclave and reacted at 220 °C for 24 h. The sample was separated by centrifugation and then washed three times with deionized water. The obtained black solid was dried in an oven at 65 °C and named MoS$_2$.

Preparation of MoS$_2$/Fe$_2$O$_3$/g-C$_3$N$_4$: MoS$_2$/Fe$_2$O$_3$/g-C$_3$N$_4$ composite catalyst was prepared by hydrothermal method. Typically, 500 mg CN and 5 mg MoS$_2$ were dissolved in 50 mL deionized water, 25 mg Fe(NO$_3$)$_3$·9H$_2$O solution and 10 mL (NH$_4$)$_2$CO$_3$ (0.5 M) solution were added in it, then the above suspension was sonicated for 30 min and transferred to an autoclave before it was hydrothermally heated at 180 °C for 12 h. When the autoclave cooled down to room temperature, the material thus obtained was separated by centrifugation and then washed three times with deionized water and dried in an oven at 65℃. Then the obtained material was ground, and the obtained light red powder was named 1%MoS$_2$/Fe$_2$O$_3$/CN (1% refers to the mass ratio of MoS$_2$ to CN). The other samples with 0.5%, 2% and 4% ratios of MoS$_2$ were prepared. Fe$_2$O$_3$ and Fe$_2$O$_3$/CN were prepared according to the above procedures. The addition ratios of Fe(NO$_3$)$_3$·9H$_2$O to CN were 3wt%, 5wt%, 10wt%, 15wt% respectively. Different ratios of Fe$_2$O$_3$/CN were named 3%Fe$_2$O$_3$/CN, 5%Fe$_2$O$_3$/CN, 10% Fe$_2$O$_3$/CN and 15% Fe$_2$O$_3$/CN.

Characterization. The structures of samples were determined on an X-ray diffractometer (XRD, 18KW/D/max2550VB/PC), the scanning range from 10°-80°. The FT-IR spectra were obtained in the range of 7800–350 cm^{-1}. A field electron emission microscope (SEM, Gemini SEM 500) and transmission electron microscope (TEM, JEM-1400) were applied to characterize the structures of the catalysts. The dates of X-ray photoelectron spectroscopy (XPS) were obtained on ESCALAB 250 (Thermo, USA) equipped with an Al Kα radiation source. The specific surface area and pore size distribution were measured through nitrogen adsorption–desorption (Angstroms/3Flex, USA) at 77 K. The UV–Vis absorption spectra ranging from 200 to 800 nm were determined by a Scan UV–Vis spectrophotometer (America, Lambda 950). The photoluminescence (PL) spectra were acquired by Fluorescence Spectrofluorometer. An electrochemical station was used to measure photocurrent responses and electrochemical impedance spectra.

Photocatalytic hydrogen production. The visible-light-induced H$_2$ release was measured in a closed photocatalytic online detection cycle system (CEL-SPH2N, Au Light, Beijing). A 300 W (λ > 400 nm) xenon lamp was selected as the visible light source. 0.05 g catalyst was stirred and dispersed in a glass container containing 20 mL sacrificial agent-Lactic acid and 80 mL distilled water. 2wt% Pt co-catalyst was photodeposited on the as-synthesized catalyst by using H$_2$PtCl$_6$·6H$_2$O as a precursor. The photocatalytic reaction system was evacuated before starting the reaction and the temperature of the reaction solution was maintained at 6 °C by the reaction of cooling water during the photocatalytic reaction. Using nitrogen as the carrier gas, the produced gas was analyzed by a gas chromatograph (GC7900) equipped with a thermal conductivity detector (TCD).

Results and discussion

Catalyst characterizations. The XRD results of CN, Fe$_2$O$_3$, MoS$_2$, Fe$_2$O$_3$/CN and MoS$_2$/Fe$_2$O$_3$/CN were depicted in Fig. 1. There were two characteristic peaks of CN、Fe$_2$O$_3$/CN and MoS$_2$/Fe$_2$O$_3$/CN at 12.78° and 27.48°, which was consistent with the (100) and (002) planes of CN (JCPDS No.87–1526)[36]. Fe$_2$O$_3$/CN and MoS$_2$/Fe$_2$O$_3$/CN composite catalyst showed the diffraction peaks of Fe$_2$O$_3$, but only two obvious characteristic peaks at 33.1°and 35.6° appeared in the composite catalyst because of the low content of Fe$_2$O$_3$, which corresponding to the (104) and (110) planes respectively[37]. Own to the weak crystallinity and ultra-thin layered structure of MoS$_2$, the typical diffraction peaks of MoS$_2$ were almost hardly observed in the MoS$_2$/Fe$_2$O$_3$/CN composite catalyst[38].

Figure 2 described the FT-IR spectra of CN, Fe$_2$O$_3$, MoS$_2$, 5%Fe$_2$O$_3$/CN and 1%MoS$_2$/Fe$_2$O$_3$/CN photocatalysts. The photocatalysts of CN, 5%Fe$_2$O$_3$/CN and 1%MoS$_2$/Fe$_2$O$_3$/CN all had the typical peaks of g-C$_3$N$_4$ in the FT-IR spectra, corresponding to the results of XRD. The characterize peaks at 1240–1650 cm^{-1} were originated
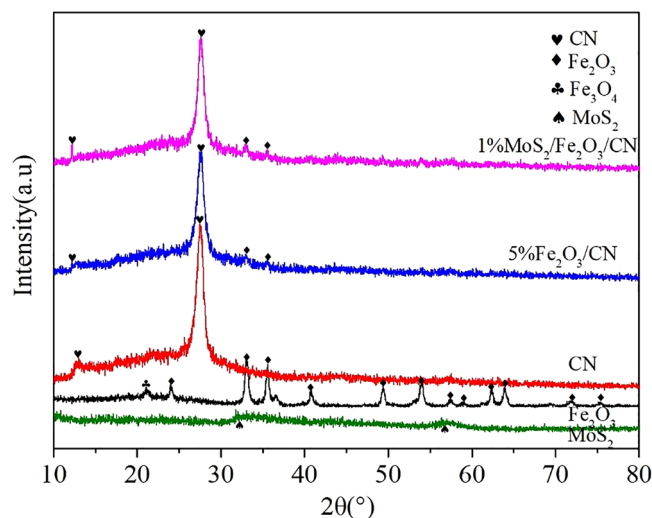
2

Figure 1. XRD pattern of CN, Fe_2O_3, MoS_2, 5%Fe_2O_3/CN and 1%MoS_2/Fe_2O_3/CN.
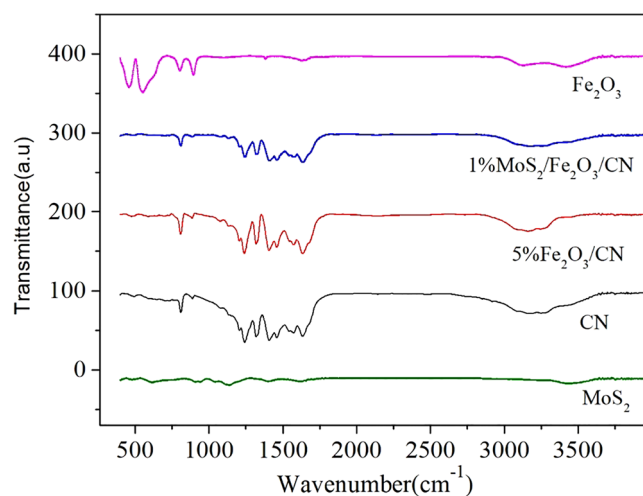
Figure 2. The FT-IR spectra of CN, Fe_2O_3, MoS_2, 5%Fe_2O_3/CN and 1%MoS_2/Fe_2O_3/CN.

from the typical C–N and C=N stretching of heterocyclic compounds. The strong peak at 810 cm^{-1} represented the triazine unit in CN[36]. The broad peak ranging from 3000 to 3300 cm^{-1} can be attributed to the N–H bond stretching of the unreacted amino group. Because of the low content of Fe_2O_3 and MoS_2, the characteristic peaks of Fe–O and Mo-S were hardly observed in the samples of 5%Fe_2O_3/CN and 1%MoS_2/5%Fe_2O_3/CN, which same as the results in XRD.

The specific morphology of the catalyst was of great significance to the study of its properties. The microscopic morphology of CN and MoS_2/Fe_2O_3/CN was acquired by SEM and the results were illustrated in Fig. 3. Figure 3a–c displayed the morphology and structure of CN at different multiples. CN was an irregular block structure, which was consistent with the literature report[39,40]. And the block structure of CN led to its small specific surface area, which was also a significant reason for its low catalytic efficiency. Figure 3d–f showed the morphology and structure of MoS_2/Fe_2O_3/CN at different multiples. The structure of the composite catalyst changed during the formation process, from the block structure to the rod structure, which was mainly attributed to the hydrothermal reaction. There were some small particles on the rod-shaped structure, but it was hard to judge whether there were traces of Fe_2O_3 and MoS_2. And it was difficult to clearly distinguish them in the SEM image because of the low content of Fe_2O_3 and MoS_2 in the composite catalyst. And the elemental composition of MoS_2/Fe_2O_3/CN was determined by energy- dispersive X-ray spectroscopy (EDS) mapping from Fig. 3g–o. From the results, elements of C, N, Fe, O, Mo and S can be captured.

The detailed structure information of the MoS_2/Fe_2O_3/CN composite catalyst were demonstrated in HRTEM, and the results were depicted in Fig. 4. Fe_2O_3 and MoS_2 form a composite catalyst with CN in the hydrothermal process. Three lattice fringes were detected in the figure of HRTEM, and the corresponding lattice spacing were 0.62 nm, 0.32 nm and 0.27 nm, which were attributed to the (002) plane of MoS_2, the (002) plane of CN and the
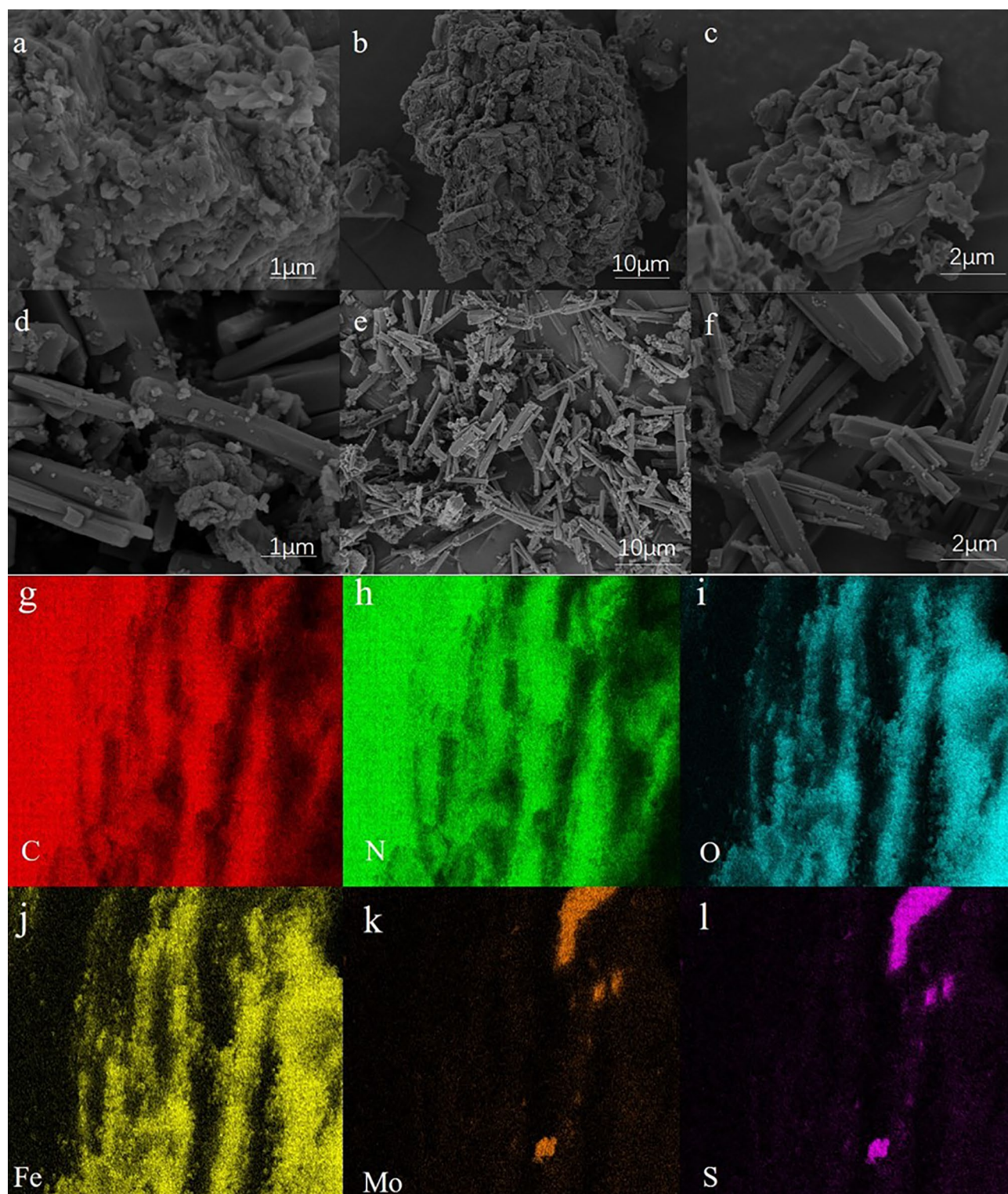
Figure 3. SEM images of CN: (**a**) 40,000×, (**b**) 5000×, (**c**) 20,000×, $MoS_2/Fe_2O_3/CN$ (**d**). 40,000×, (**e**) 5000×, (**f**) 20,000×, and the corresponding elements mapping of $MoS_2/Fe_2O_3/CN$.

(110) plane of Fe_2O_3[31,41,42]. The positional combination of the three materials provided evidence for the charge transfer pathway of the photocatalytic mechanism.

Because of the small content of Fe_2O_3 and MoS_2 in the composite catalyst, it was hard to find information of them in SEM, XRD and FT-IR, but the successful combination of Fe_2O_3, MoS_2 and CN were proved in EDS and HRTEM results. In order to further explore the characteristics of $MoS_2/Fe_2O_3/CN$, the element composition and chemical state of the $MoS_2/Fe_2O_3/CN$ composite catalyst were acquired through XPS. The XPS spectrums
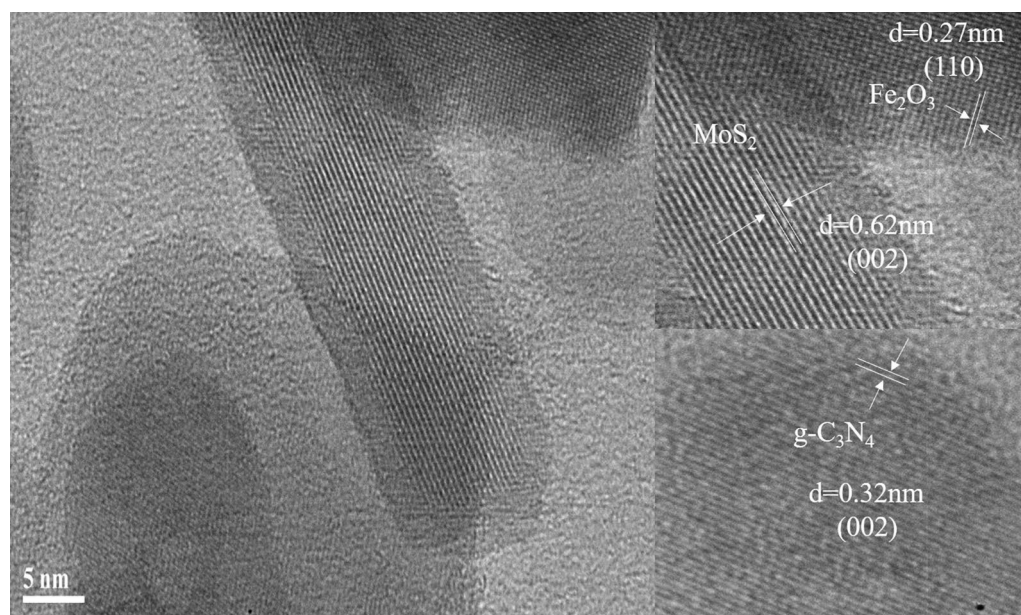
Figure 4. The HRTEM images of $MoS_2/Fe_2O_3/CN$ composite catalyst.

of various elements were demonstrated in Fig. 5, and some vestige of Fe_2O_3 and MoS_2 were found in the XPS spectrums. There were two peaks at 284.8 eV and 288.2 eV in C 1s spectrum, which consistent with the bond of C–C and N=C–N respectively[43]. Figure 5b illustrated the N 1s spectrum of the composite catalyst, it contained three peaks at 398.7 eV, 399.7 eV and 401 eV. The peak at 398.7 eV was caused by sp^{2-} heterozygosity N in C=N–C. The peak at 399.7 eV corresponded to the sp^{3-} hybridization of N in $N–(C)_3$, while the peak at 401.1 eV was arose from N–C-H in the amino group. The O 1s spectrum appeared three characteristic peaks at 529.7 eV, 531.3 eV and 532.3 eV, which can be ascribed to the O^{2-} in Fe_2O_3, hydroxyl in the surface and the adsorption of H_2O[37,44]. The Fe 2p spectrum had four peaks at 710.24 eV, 711.35 eV, 717.28 eV and 723.8 eV. 711.35 eV and 723.8 eV corresponded to the binding energies of Fe $2p_{5/2}$ and Fe $2p_{1/2}$, which were consistent with Fe^{3+} in Fe_2O_3. The two satellite peaks at 710.24 eV, 717.28 eV were caused by the charge migration of Fe^{3+}[44–46]. The two peaks at 228 eV, 231.8 eV in Mo 2p spectrum can be attributed to Mo $3d_{5/2}$ and $3d_{3/2}$, indicating that the existence of Mo^{4+}[33]. The peak at 235.3 eV was corresponded to the Mo–O bond of Mo 6p, which was formed by the combination of Mo atoms and O in Fe_2O_3[47]. The XPS spectrum of S 2p was displayed in Fig. 5d, the characteristic peaks at 161.3 eV and 162.6 eV have corresponded to S $2p_{3/2}$ and S $2p_{1/2}$ of S^{2-}. The peak at 168.31 eV belonged to the edge unsaturated S atom of the ultra-thin layer, which was considered to be the active site for hydrogen production and was the unique flake modification advantage of MoS_2[47]. The unique advantage of MoS_2 lied in the presence of edge unsaturated S atom, which provided more reaction site to improve the hydrogen production. The binding energy corresponding to the unsaturated S atom was 168.31 eV.

Figure 6 depicted the UV–Vis diffuse reflectance spectra of CN, Fe_2O_3, MoS_2, Fe_2O_3/CN and $MoS_2/Fe_2O_3/CN$ composite catalysts. In the range of 300–450 nm, the catalyst of CN had higher absorption and appeared an absorption edge at about 456 nm. The UV absorption spectrum of the Fe_2O_3/CN composite catalyst was similar to the main absorption edge of CN. The composite catalyst had two absorption band edges, which were consistent with the UV absorption spectrum of Fe_2O_3. The composite catalyst exhibited stronger absorption, especially under visible light, and the absorption curve shifted significantly to longer wavelengths. After MoS_2 loaded to Fe_2O_3/CN composite catalyst, the absorption of visible light by the composite catalyst had been further improved. The band gap value of the photocatalyst was determined by the following formula.

$$\alpha h\nu = A(h\nu - E_g)^{n/2}$$

where α, hν, and E_g refers to absorption coefficient, photon energy and band gap, respectively. A is a constant, n = 1 means a direct band gap while n = 4 refers to an indirect band gap[48]. According to the equation, the band gaps of CN, Fe_2O_3/CN and $MoS_2/Fe_2O_3/CN$ can be roughly estimated, the results were shown in Fig. 6b. According to the formula, the band gap of CN was predicted to be 2.84 eV. Besides, the band gap values of the composite catalysts $5\%Fe_2O_3/CN$ and $1\%MoS_2/Fe_2O_3/CN$ were 2.76 eV and 2.79 eV according to the prediction. The band gap of the synthesized composite catalysts were reduced, which were beneficial to the catalyst to further absorb sunlight and improve the photocatalytic performance.

Table 1 described the specific surface area of CN, $5\%Fe_2O_3/CN$ and $1\%MoS_2/Fe_2O_3/CN$. As illustrated, the specific surface area of $1\%MoS_2/Fe_2O_3/CN$ was 61.76 m^2/g, which was the highest among all catalysts, consistent with the results of the highest H_2 production rate discussed below. The specific surface area of the composite catalyst was increased mainly due to the change of the composite catalyst in structure, from the original block structure to a rod-like structure during the hydrothermal reaction process. This structure can provide more
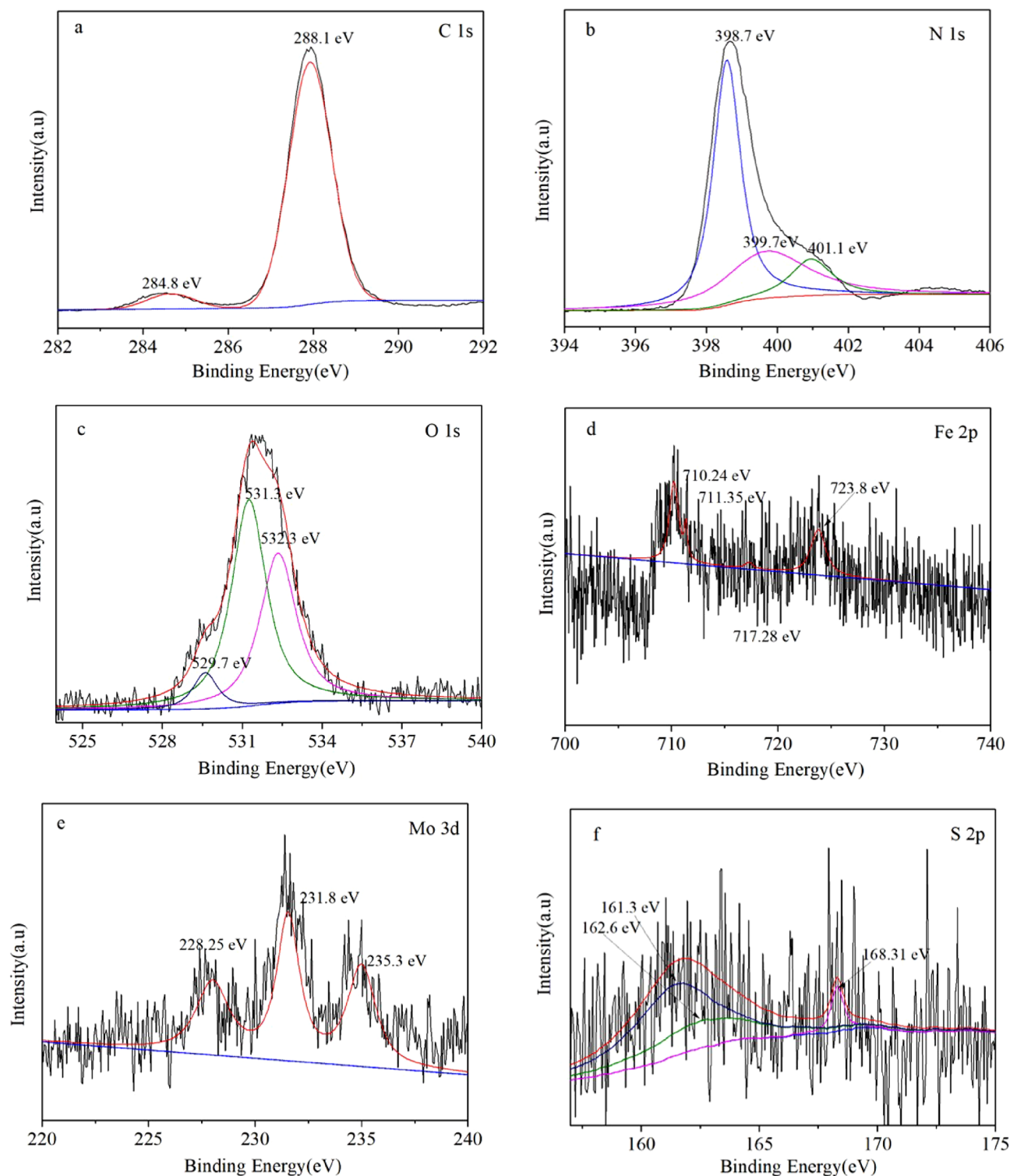
Figure 5. XPS spectra of 1%MoS$_2$/Fe$_2$O$_3$/CN, (**a**) C 1s spectrum, (**b**) N 1s spectrum, (**c**) O 1s spectrum, (**d**) Fe 2p spectrum, (**e**) Mo 3d spectrum, (**f**) S 2p spectrum.

sites for the catalytic reactions. And the addition of MoS$_2$ increased the number of micropores in the composite catalyst, thereby further increasing the specific surface area of the composite catalyst. As we all know that the specific surface area was one of the main reasons influencing the performance of the photocatalyst. High specific surface area can provide more active sites for photocatalytic reaction and the existence of the pore structure provide more carrier charge transfer channels, which helped to improve the photocatalytic activity. The nitrogen adsorption–desorption isotherms of CN, 5%Fe$_2$O$_3$/CN and 1%MoS$_2$/Fe$_2$O$_3$/CN were demonstrated in Fig. 7. According to the classification of IUPAC, the adsorption–desorption isotherm of the photocatalysts of CN,
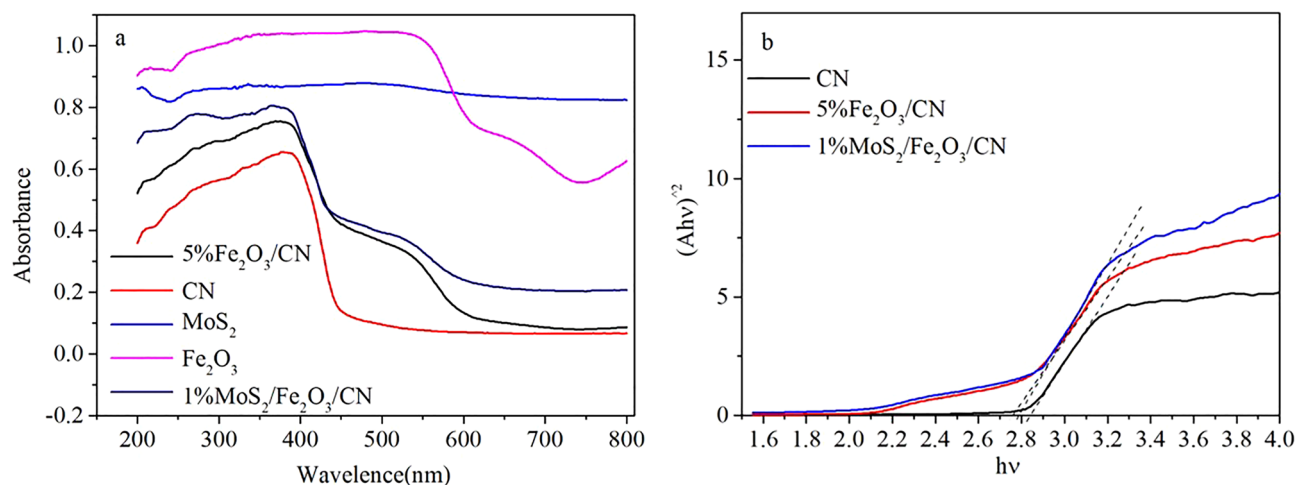
Figure 6. (**a**) UV–Vis absorption spectrum of photocatalysts (**b**) band gap diagram of photocatalysts.

Sample	CN	5%Fe$_2$O$_3$/CN	1%MoS$_2$/Fe$_2$O$_3$/CN
S$_{BET}$ (m^2/g)	14.55	38.36	61.76

Table 1. The specific surface areas of CN, 5%Fe$_2$O$_3$/CN and 1%MoS$_2$/Fe$_2$O$_3$/CN.
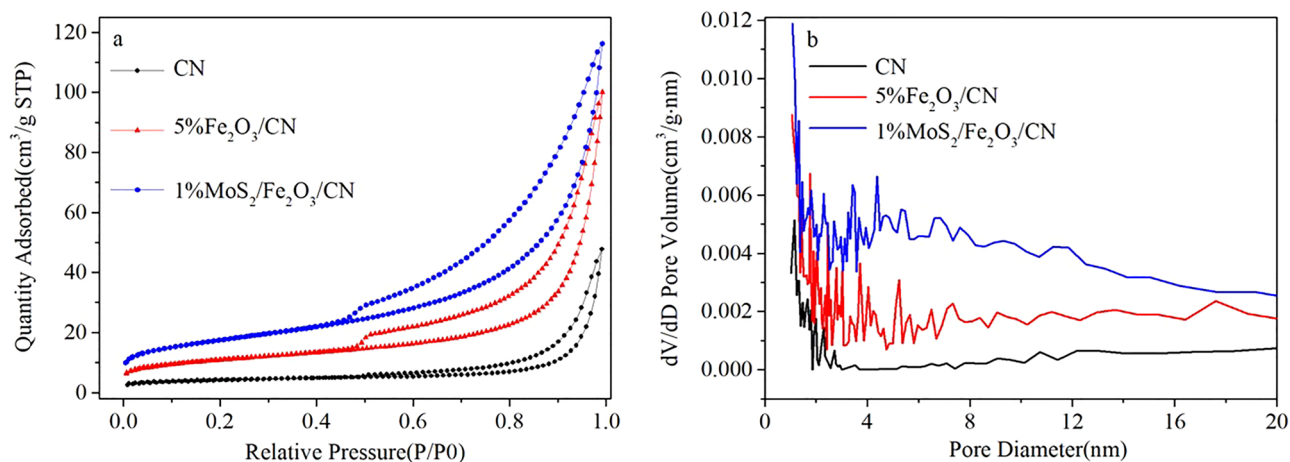
Figure 7. N$_2$ adsorption–desorption isotherms and pore size distributions of CN, 5%Fe$_2$O$_3$/CN, and 1% MoS$_2$/Fe$_2$O$_3$/CN.

5%Fe$_2$O$_3$/CN and 1%MoS$_2$/Fe$_2$O$_3$/CN was type IV, and the types of hysteresis loop were H3. As depicted, when the relative pressure was in the range of 0.8–1.0, the adsorption–desorption isotherm appears higher absorption, which meant that the catalyst had a porous structure.

To compare the carrier separation efficiency of different photocatalysts, CN, 5%Fe$_2$O$_3$/CN and 1%MoS$_2$/Fe$_2$O$_3$/CN were characterized by photoluminescence spectroscopy and time-resolved PL spectra, the results were described in Fig. 8a, b. The PL spectrum can display the photogenerated electron–hole separation ability of the prepared composite catalyst. Generally, the stronger the spectrum intensity of the PL, the lower the separation efficiency of the photocatalyst carriers. The PL spectrum of pure CN had very high fluorescence intensity in the range of 420–550 nm, which was about 4 times higher than the composite catalyst MoS$_2$/Fe$_2$O$_3$/CN. It meant that the pure CN had weaker carrier mobility than the composite catalyst, and photo-generated electron–hole was more likely to occur complex. The fluorescence intensity of the MoS$_2$/Fe$_2$O$_3$/CN composite catalyst was the weakest, indicating it had the highest carrier separation efficiency and lowest probability of photo-generated electron–hole recombination among all photocatalysts. Time-resolved PL spectroscopy further demonstrates the characteristics of charge carrier lifetime. The average lifetime of MoS$_2$/Fe$_2$O$_3$/CN was 4.954 ns, which shorter than CN (5.717 ns) and Fe$_2$O$_3$/CN (5.538 ns), it meant MoS$_2$/Fe$_2$O$_3$/CN can effectively inhibit the recombination
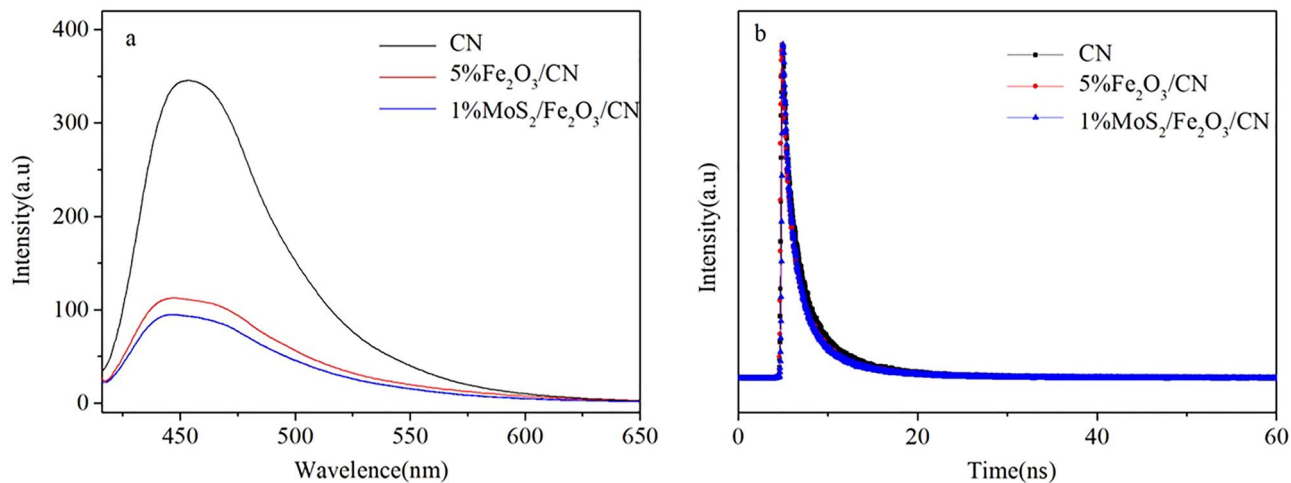
Figure 8. The PL spectrum (**a**) and fluorescence decay curves (**b**) of CN, 5%Fe_2O_3/CN and 1%MoS_2/Fe_2O_3/CN.
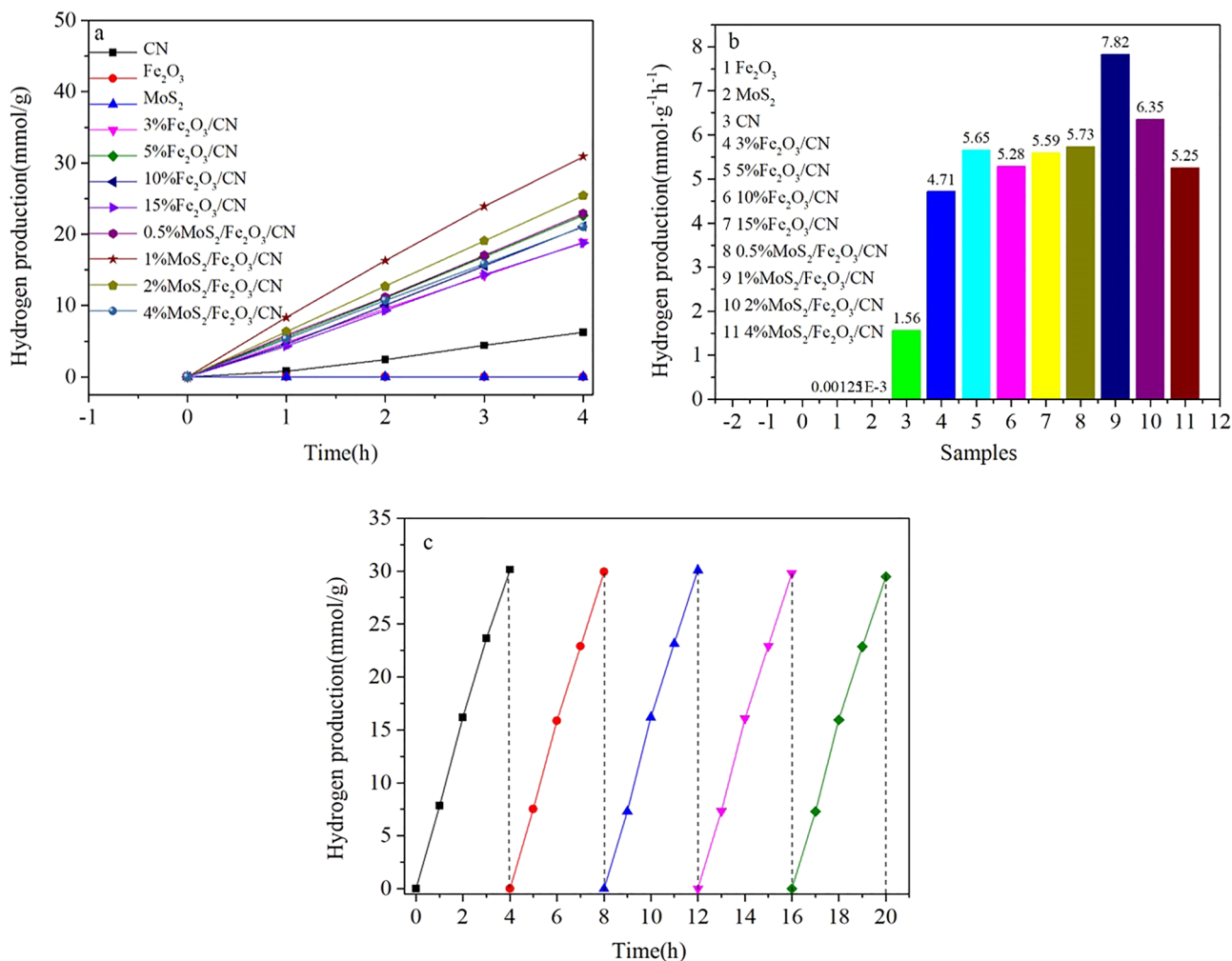

Figure 9. (**a**) The Hydrogen accumulation of different samples, (**b**) the Hydrogen producton rate of different samples, (**c**) the hydrogen production cycle of 1%MoS_2/Fe_2O_3/CN composite catalyst.
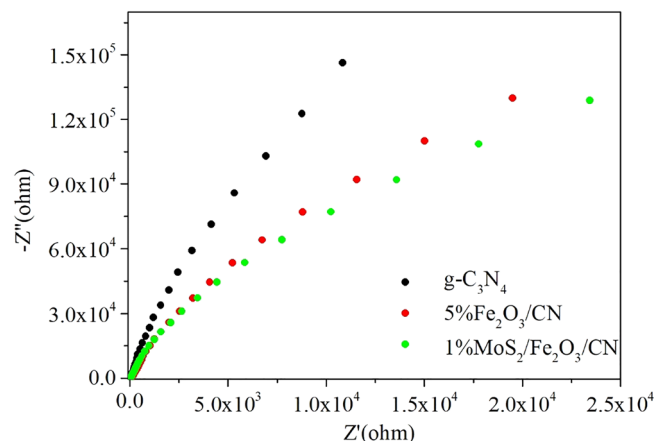
Figure 10. Electrochemical impedance spectra of samples.

of electron and hole. The PL and time-resolved PL spectra results were consistent with the conclusion of the hydrogen production test.

Under visible light condition, the hydrogen production rate of $MoS_2/Fe_2O_3/CN$ composite catalyst was shown in Fig. 9, including the control groups. The hydrogen production rate of pure CN was 1.56 mmol g^{-1} h^{-1}, while the rates of Fe_2O_3 and MoS_2 were relatively low, which can be almost ignored. Fe_2O_3/CN composite catalyst demonstrated enhanced hydrogen release performance and the 5%Fe_2O_3/CN photocatalyst showed the best hydrogen production rate, which was 5.65 mmol g^{-1} h^{-1}. After loading MoS_2 on the Fe_2O_3/CN composite catalyst, the photocatalytic hydrogen production rate of the composite catalyst was further improved. The highest hydrogen production rate of 1%MoS_2/Fe_2O_3/CN composite catalyst was 7.82 mmol g^{-1} h^{-1}, which was about 5 times higher than that of pure CN (1.56 mmol g^{-1} h^{-1}) and 1.38 times higher than 5%Fe_2O_3/CN. The reusability and stability of the catalyst were considered to be important practical evaluation and application parameters. In this paper, using MoS_2/Fe_2O_3/CN as the photocatalyst, five consecutive cycles of experiments were conducted to explore the stability of hydrogen evolution. As displayed in Fig. 9c, the hydrogen generation rate was still stable after five cycles, indicating the good stability and sustainable utilization of the photocatalyst.

Electrochemical characterization. An electrochemical impedance spectroscopy test was carried out to evaluate the charge transfer capability of the photocatalyst, and the results were demonstrated in Fig. 10. As described in Fig. 10, the resistance of pure CN was relatively large, which hindered its charge transfer. After being combined with 5% Fe_2O_3, the resistance of the composite catalyst was greatly decreased. When the catalyst was further combined with MoS_2, the charge transfer resistance of the composite catalyst was further decreased. It was known that when the resistance of electrochemical impedance was smaller, the resistance of charge transfer was lower, the photocatalytic activity was better. The results of PL demonstrated that the charge transferability of the MoS_2/Fe_2O_3/CN composite catalyst was improved, thus the photocatalytic performance was improved.

The test of transient photocurrent response was an effective way to evaluate the carrier mobility of photocatalysts. And the photocurrent responses diagrams of CN, 5%Fe_2O_3/CN and 1%MoS_2/Fe_2O_3/CN photocatalysts were shown in Fig. 11. The photocurrent responses current of the composite catalyst 1%MoS_2/Fe_2O_3/CN was significantly higher than the catalysts of 5%Fe_2O_3/CN and CN, which implied that its electron–hole separation efficiency was the highest among the samples. And the results also illustrated that the photocatalytic activity of the composite catalyst was the best, which was consistent with the results of PL and EIS.

Photocatalytic mechanism. In order to explore the process mechanism of photocatalytic hydrogen production, the EPR characterization technology was used to detect the free radicals in the photocatalytic process. The test results were shown in Fig. 12 and the EPR signals of ·OH and ·O_2^- were shown in Fig. 12a, b, respectively. The results demonstrated that signals of ·OH and ·O_2^- were existed in the system of MoS_2/Fe_2O_3/CN and the peak intensity of MoS_2/Fe_2O_3/CN was the highest, which indicated that the catalytic mechanism of the ternary composite catalyst can be represented by Z-scheme. Based on the EPR and HRTEM results, the possible photocatalytic mechanism of the MoS_2/Fe_2O_3/CN composite catalyst was illustrated in Fig. 13. The band gap structures of g-C_3N_4, Fe_2O_3 and MoS_2 were determined by previous studies[49,50]. Under the condition of light, electrons were generated in the valence bands of CN、Fe_2O_3 and MoS_2, the electrons transferred from the valence band to the conduction band, and holes were generated in the valence band. It was known from the literature that if the reaction was based on the traditional heterojunction electron transfer mechanism, the active materials ·OH and ·O_2^- cannot be produced due to the potential of CN、Fe_2O_3 and MoS_2[46], which was inconsistent with the EPR test results in Fig. 12. Therefore, based on the previously reported literature, in this paper, we explained the photocatalytic performance of the composite catalyst through the Z-type heterojunction mechanism. In this system, the electrons in the Fe_2O_3 conduction band were transferred to the valence band of CN under the action of the intermediary MoS_2, which consumed the holes and reduced the photo-generated electron–hole recombination in CN. The sacrificial agent lactic acid was oxidized on the valence band of Fe_2O_3, consuming holes and
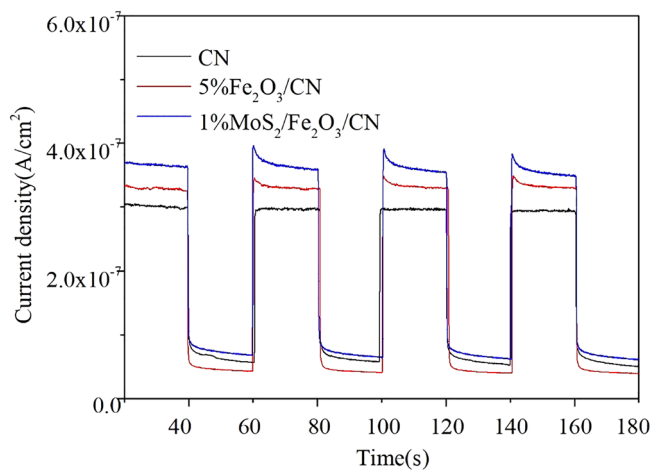
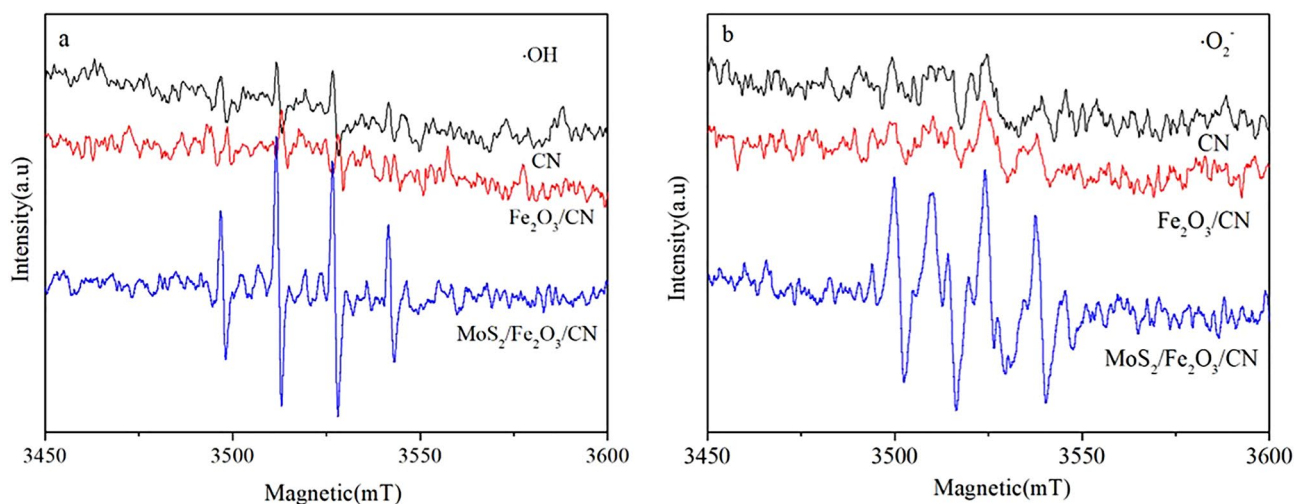**Figure 11.** Transient photocurrent responses of photocatalysts.

Figure 12. EPR spectra of CN, Fe_2O_3/CN and MoS_2/Fe_2O_3/CN in different system under visible light. (**a**) $DMPO-\cdot OH$ in water, (**b**) $DMPO-\cdot O_2^-$ in methanol in the system.
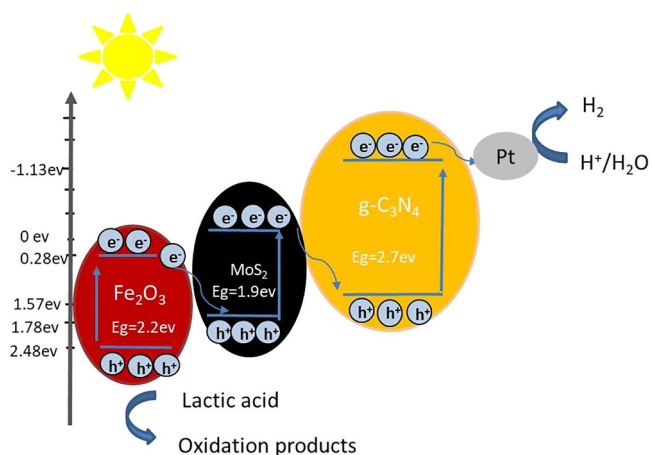

Figure 13. The photocatalytic mechanism of 1%MoS_2/Fe_2O_3/CN composite catalyst.

accelerating the migration of carriers. Under the action of the co-catalyst MoS_2 and Pt, the active sites of CN can effectively produce hydrogen.

Conclusions

In conclusion, the ternary composite catalyst $MoS_2/Fe_2O_3/CN$ was successfully prepared through the hydrothermal method, and a series of characterizations confirmed that the composite catalyst has the superior photocatalytic performance among the samples. The various characterization results demonstrated that with the addition of Fe_2O_3 and MoS_2, the ternary composite catalyst $MoS_2/Fe_2O_3/CN$ had a larger specific surface area, stronger visible light absorption capacity, higher carrier migration efficiency, and lower photogenerated electron–hole recombination rate. And $MoS_2/Fe_2O_3/CN$ showed higher hydrogen production activity, reaching 7.82 mmol g^{-1} h^{-1}, which was about 5 times higher than the basic catalyst CN. The Z-scheme photocatalytic process was testified by EPR analysis and the research on the composite catalyst $MoS_2/Fe_2O_3/CN$ provided some useful reference information for the development of other ternary composite catalysts.

References

1. Wang, Z., Huang, X. & Wang, X. Recent progresses in the design of $BiVO_4$-based photocatalysts for efficient solar water splitting. *Catal. Today* **335**, 31–38 (2019).
2. Guo, H. *et al.* Synthesis of Z-scheme α-Fe_2O_3/g-C_3N_4 composite with enhanced visible-light photocatalytic reduction of CO_2 to CH_3OH. *J. CO2 Util.* **33**, 233–241 (2019).
3. Dong, Z., Wu, Y., Thirugnanam, N. & Li, G. Double Z-scheme ZnO/ZnS/ g-C_3N_4 ternary structure for efficient photocatalytic H_2 production. *Appl. Surf. Sci.* **430**, 293–300 (2018).
4. Kahng, S., Yoo, H. & Kim, J. H. Recent advances in earth-abundant photocatalyst materials for solar H_2 production. *Adv. Powder Technol.* **31**(1), 11–28 (2020).
5. Zhang, X., Li, L., Zhou, Q., Liang, X. & Liu, D. Facile synthesis of novel gully-like double-sized mesoporous structural Sr-doped ZrO_2–TiO_2 composites with improved photocatalytic efficiency. *J. Solid State Chem.* **269**, 375–385 (2019).
6. Bo, T., Yuan, J., Liu, Y., Cao, S. & Zhou, W. Activated edge of single layered TiO_2 nanoribbons through transition metal doping and strain approaches for hydrogen production. *Appl. Surf. Sci.* **545**, 148947 (2021).
7. Ismael, M. Enhanced photocatalytic hydrogen production and degradation of organic pollutants from Fe (III) doped TiO_2 nanoparticles. *J. Environ. Chem. Eng.* **8**(2), 103676 (2020).
8. Lin, K. *et al.* Improved photocatalytic hydrogen evolution on (Ru/WC)/CdS via modulating the transferring paths of photo-excited electrons. *Appl. Catal. B Environ.* **286**, 119880 (2021).
9. Yang, H. *et al.* Drastic promotion of the photoreactivity of MOF ultrathin nanosheets towards hydrogen production by deposition with CdS nanorods. *Appl. Catal. B Environ.* **285**, 119801 (2021).
10. Zhuge, K. *et al.* In-suit photodeposition of MoS_2 onto CdS quantum dots for efficient photocatalytic H_2 evolution. *Appl. Surf. Sci.* **539**, 148234 (2021).
11. Galdámez-Martínez, A., Bai, Y., Santana, G., Sprick, R. S. & Dutt, A. Photocatalytic hydrogen production performance of 1-D ZnO nanostructures: role of structural properties. *Int. J. Hydrog. Energy* **45**(56), 31942–31951 (2020).
12. Haddad, M., Belhadi, A., Boudjellal, L. & Trari, M. Photocatalytic hydrogen production on the hetero-junction CuO/ZnO. *Int. J. Hydrog. Energy* **46**, 37556 (2020).
13. Patil, R. P., Mahadik, M. A., Chae, W.-S., Choi, S. H. & Jang, J. S. Self-templated fabrication of 2-D dual nanoarchitecture Zn1-xCdxS porous nanosheet and ZnO nanorod for photoelectrochemical hydrogen production. *Appl. Surf. Sci.* **539**, 148267 (2021).
14. Deng, P., Hong, W., Cheng, Z., Zhang, L. & Hou, Y. Facile fabrication of nickel/porous g-C3N4 by using carbon dot as template for enhanced photocatalytic hydrogen production. *Int. J. Hydrog. Energy* **45**(58), 33543–33551 (2020).
15. Hu, Z., Lyu, J. & Ge, M. Role of reactive oxygen species in the photocatalytic degradation of methyl orange and tetracycline by Ag_3PO_4 polyhedron modified with g-C_3N_4. *Mater. Sci. Semicond. Process.* **105**, 104731 (2020).
16. Chen, Z. *et al.* 1D metallic MoO_2-C as co-catalyst on 2D g-C_3N_4 semiconductor to promote photocatlaytic hydrogen production. *Appl. Surf. Sci.* **447**, 732–739 (2018).
17. Li, Y., Zhou, M., Cheng, B. & Shao, Y. Recent advances in g-C_3N_4-based heterojunction photocatalysts. *J. Mater. Sci. Technol.* **56**, 1–17 (2020).
18. Liu, G. *et al.* Comparative study of pure g-C_3N_4 and sulfur-doped g-C_3N_4 catalyst performance in photo-degradation of persistent pollutant under visible light. *J. Nanosci. Nanotechnol.* **18**(6), 4142–4154 (2018).
19. Lin, Q. *et al.* Controlled preparation of P-doped g-C_3N_4 nanosheets for efficient photocatalytic hydrogen production. *Chin. J. Chem. Eng.* **28**(10), 2677–2688 (2020).
20. Liu, G., Xue, M., Liu, Q., Yang, H. & Zhou, Y. Facile synthesis of C-doped hollow spherical g-C3N4 from supramolecular self-assembly for enhanced photoredox water splitting. *Int. J. Hydrog. Energy* **44**(47), 25671–25679 (2019).
21. Che, H. *et al.* Nitrogen doped carbon ribbons modified g-C_3N_4 for markedly enhanced photocatalytic H_2-production in visible to near-infrared region. *Chem. Eng. J.* **382**, 122870 (2020).
22. Sun, S. *et al.* Facile constructing of isotype g-C_3N_4(bulk)/g-C_3N_4(nanosheet) heterojunctions through thermal polymerization of single-source glucose-modified melamine: an efficient charge separation system for photocatalytic hydrogen production. *Appl. Surf. Sci.* **500**, 143985 (2020).
23. Wang, Y. *et al.* One-pot synthesis of K-doped g-C_3N_4 nanosheets with enhanced photocatalytic hydrogen production under visible-light irradiation. *Appl. Surf. Sci.* **440**, 258–265 (2018).
24. Dong, F. *et al.* Efficient synthesis of polymeric g-C_3N_4 layered materials as novel efficient visible light driven photocatalysts. *J. Mater. Chem.* **21**(39), 15171–15174 (2011).
25. Hao, X. *et al.* Zn-vacancy mediated electron-hole separation in ZnS/g-C_3N_4 heterojunction for efficient visible-light photocatalytic hydrogen production. *Appl. Catal. B Environ.* **229**, 41–51 (2018).
26. Pan, J. *et al.* The enhancement of photocatalytic hydrogen production via Ti3+ self-doping black TiO_2/g-C_3N_4 hollow core-shell nano-heterojunction. *Appl. Catal. B Environ.* **242**, 92–99 (2019).
27. Zhu, Y., Wan, T., Wen, X., Chu, D. & Jiang, Y. Tunable Type I and II heterojunction of CoOx nanoparticles confined in g-C_3N_4 nanotubes for photocatalytic hydrogen production. *Appl. Catal. B Environ.* **244**, 814–822 (2019).
28. Liu, J. *et al.* Amorphous NiO as co-catalyst for enhanced visible-light-driven hydrogen generation over g-C_3N_4 photocatalyst. *Appl. Catal. B Environ.* **222**, 35–43 (2018).
29. Tong, M., Sun, D., Zhang, R., Liu, H. & Chen, R. Preparation of Si–α-Fe_2O_3/CdS composites with enhanced visible-light photocatalytic activity for p-nitrophenol degradation. *J. Alloys Compd.* **862**, 158271 (2021).

30. Xiong, S. *et al.* One-step preparation of well-dispersed spindle-like Fe_2O_3 nanoparticles on g-C3N4 as highly efficient photocatalysts. *Ecotoxicol. Environ. Saf.* **208**, 111519 (2021).
31. Zhao, H., Tian, C., Mei, J., Yang, S. & Wong, P. K. Faster electron injection and higher interface reactivity in g-C$_3$N$_4$/Fe$_2$O$_3$ nano-hybrid for efficient photo-Fenton-like activity toward antibiotics degradation. *Environ. Res.* **195**, 110842 (2021).
32. Zhang, R. *et al.* An effective method to understand photo-generated charge transfer processes of Z-scheme Ti/α-Fe$_2$O$_3$/g-C$_3$N$_4$ photocatalysts for hydrogen evolution. *Catal. Commun.* **142**, 106028 (2020).
33. Zhang, X., Zhang, R., Niu, S., Zheng, J. & Guo, C. Enhanced photo-catalytic performance by effective electron-hole separation for MoS$_2$ inlaying in g-C$_3$N$_4$ hetero-junction. *Appl. Surf. Sci.* **475**, 355–362 (2019).
34. Sun, J. *et al.* Two-dimensional/one-dimensional molybdenum sulfide (MoS$_2$) nanoflake/graphitic carbon nitride (g-C$_3$N$_4$) hollow nanotube photocatalyst for enhanced photocatalytic hydrogen production activity. *J. Colloid Interface Sci.* **567**, 300–307 (2020).
35. Zhang, Z. *et al.* Synthesis of flower-like MoS$_2$/g-C$_3$N$_4$ nanosheet heterojunctions with enhanced photocatalytic reduction activity of uranium(VI). *Appl. Surf. Sci.* **520**, 146352 (2020).
36. Ghane, N., Sadrnezhaad, S. K. & Hosseini, H. S. M. Combustion synthesis of g-C$_3$N$_4$/Fe$_2$O$_3$ nanocomposite for superior photo-electrochemical catalytic performance. *Appl. Surf. Sci.* **534**, 147563 (2020).
37. Bakr, A. E. A. *et al.* Synthesis and characterization of Z-scheme α-Fe$_2$O$_3$ NTs/ruptured tubular g-C3N4 for enhanced photoelec-trochemical water oxidation. *Sol. Energy* **193**, 403–412 (2019).
38. Mu, H. *et al.* Novel polymer supported graphene and molybdenum sulfide as highly efficient cocatalyst for photocatalytic hydrogen evolution. *Int. J. Hydrog. Energy* **43**(39), 18105–18114 (2018).
39. Palanivel, B. *et al.* Inverse spinel NiFe$_2$O$_4$ deposited g-C$_3$N$_4$ nanosheet for enhanced visible light photocatalytic activity. *Mater. Sci. Semicond. Process.* **100**, 87–97 (2019).
40. Wang, W. *et al.* Halloysite-derived mesoporous g-C$_3$N$_4$ nanotubes for improved visible-light photocatalytic hydrogen evolution. *Appl. Clay Sci.* **158**, 143–149 (2018).
41. Raza, A., Shen, H., Haidry, A. A. & Cui, S. Hydrothermal synthesis of Fe$_3$O$_4$/TiO$_2$/g-C$_3$N$_4$: advanced photocatalytic application. *Appl. Surf. Sci.* **488**, 887–895 (2019).
42. Du, C. *et al.* Enhanced electrocatalytic hydrogen evolution performance of MoS$_2$ ultrathin nanosheets via Sn doping. *Appl. Catal. A Gen.* **538**, 1–8 (2017).
43. Lan, Z.-A., Zhang, G. & Wang, X. A facile synthesis of Br-modified g-C$_3$N$_4$ semiconductors for photoredox water splitting. *Appl. Catal. B Environ.* **192**, 116–125 (2016).
44. Li, Y. *et al.* Synthesis of α-Fe$_2$O$_3$/g-C$_3$N$_4$ photocatalyst for high-efficiency water splitting under full light. *Mater. Des.* **196**, 109191 (2020).
45. Bai, J. *et al.* Facile fabrication of α-Fe$_2$O$_3$/porous g-C$_3$N$_4$ heterojunction hybrids with enhanced visible-light photocatalytic activity. *Mater. Chem. Phys.* **234**, 75–80 (2019).
46. Geng, Y. *et al.* Z-Scheme 2D/2D α-Fe$_2$O$_3$/g-C$_3$N$_4$ heterojunction for photocatalytic oxidation of nitric oxide. *Appl. Catal. B Environ.* **280**, 119409 (2021).
47. Pan, J. *et al.* The photocatalytic hydrogen evolution enhancement of the MoS$_2$ lamellas modified g-C$_3$N$_4$/SrTiO$_3$ core-shell hetero-junction. *Renew. Energy* **161**, 340–349 (2020).
48. Han, X. *et al.* WO$_3$/g-C$_3$N$_4$ two-dimensional composites for visible-light driven photocatalytic hydrogen production. *Int. J. Hydrog. Energy* **43**(10), 4845–4855 (2018).
49. Li, Y.-P. *et al.* Z-scheme electronic transfer of quantum-sized α-Fe$_2$O$_3$ modified g-C$_3$N$_4$ hybrids for enhanced photocatalytic hydrogen production. *Int. J. Hydrog. Energy* **42**(47), 28327–28336 (2017).
50. Yuan, Y. *et al.* Recent advances and perspectives of MoS2-based materials for photocatalytic dyes degradation: a review. *Colloids Surf. A Physicochem. Eng. Asp.* **611**, 125836 (2021).

Author contributions

Y.Z.: experiments, data analysis, writing-original draft. C.Z.: auxiliary experiments. J.W.: writing and supervision. X.C.: writing supervision, project administration and funding acquisition.

Competing interests

The authors declare no competing interests.

Additional information

Correspondence and requests for materials should be addressed to X.C.

Reprints and permissions information is available at www.nature.com/reprints.

Publisher's note Springer Nature remains neutral with regard to jurisdictional claims in published maps and institutional affiliations.